Multifractal characterization of femtosecond laser-induced herringbone patterns

IOP Publishing J. Phys. Photonics 3 (2021) 015001 https://doi.org/10.1088/2515-7647/abcb73

Journal of Physics: Photonics

OPEN ACCESS

RECEIVED
24 September 2020

REVISED
31 October 2020

ACCEPTED FOR PUBLICATION
11 November 2020

PUBLISHED
14 December 2020

PAPER

Multifractal characterization of femtosecond laser-induced herringbone patterns

Vramori Mitra[1,3], **Erik M Garcell**[1,3], **Mohamed ElKabbash**[1,3], **Anupam Neogi**[2] **and Chunlei Guo**[1]

[1] The Institute of Optics, University of Rochester, Rochester, NY 14627, United States of America
[2] Department of Mechanical Engineering, University of Rochester, Rochester, NY 14627, United States of America
[3] These authors contributed equally to this work.

E-mail: guo@optics.rochester.edu

Keywords: fractal analysis, laser induced periodic surface structures, femtosecond laser processing

Abstract

Analysis of surface structures formed due to femtosecond laser surface ablation is usually done through subjective assessment of the surface images. Here, we analyze the evolution of femtosecond laser-induced surface structures using multifractal analysis. We computed the singularity spectrum to characterize the behavior of laser-induced herringbone patterns. The surface morphology of the ablated surface shows a polarization dependent multifractal nature. The singularity spectrum depicts three distinct morphological phases that sequentially form as a function of the laser pulse number. We objectively characterize the laser-dependent morphological properties of herringbone structures. Multifractal analysis was able to reflect the hierarchy, uniformity, and roughness of the formed structures and their dependence on the pulse number and polarization.

Fractal geometry provides a mathematical description of how the complexity of a system scales with its size [1]. Fractal patterns are ubiquitous; they appear in snowflakes, coastlines, clouds, the structure of the nervous system, and even in the movements of global financial markets. Over the past decades, fractal analysis has received great research interest for image compression, texture analysis, texture image segmentation and surface roughness [2–6]. In particular, multifractal analysis is employed to characterize objects with varying fractal properties over multiple scales.

On the other hand, ultrafast laser-matter interactions are complex [7, 8] and can exhibit several ablation dynamics including phase explosions, fragmentation, and spallation [9]. The degree of uniformity, periodicity, and complexity depend on the laser parameters and material properties [9–11]. Here, we perform multifractal analyses on femtosecond laser-induced surface structures. As a case study, we analyze the evolution of the so-called herringbone structures [12, 13] which undergoes a multitude of polarization and pulse number dependent morphological phases. Our main goal is to introduce the study of multifractal geometries to characterize unique laser ablated features which provides a deeper understanding of the physics underlying their structural evolution. The multifractal analysis is particularly useful to analyze seemingly random surface topographies. In addition, as we elucidate later, multifractal analysis captures the dependence of surface characteristics on scale which is of major relevance to the study of hierarchical structures.

When the fractal dimension of a pattern changes within consecutive ranges of scale, one generally invokes the notion of multifractality. Multifractal objects are expressed by several fractal dimension in different regions i in contrast to a mono-fractal object which has a single fractal dimension. Fractal objects exhibit details at arbitrarily small scales that are often too complex to be represented in a Euclidean space. Fractal analysis gives insight into the distribution of these complex systems. In a homogeneous system, the probability P of a measure scales with the size, or scale as $P(\varepsilon) \sim \varepsilon^{D}$, where D is the fractal dimension of the system and is given by $\mathrm{D} = \lim_{\varepsilon \to 0} \log N(\varepsilon) / \log(1/\varepsilon)$ [14, 15], where $N(\varepsilon)$ is the number of boxes required to cover the system. Separating the system into boxes of side length ε, we can count the number of boxes required to cover a given geometry. Accordingly, the fractal dimension of an object is a measure of the density of the fractal in the space it occupies. Note that other methods of calculating the fractal dimension exist [16, 17]. The fractal dimension of Euclidean objects has an integer value, e.g. 1 for a line, 2 for a surface,

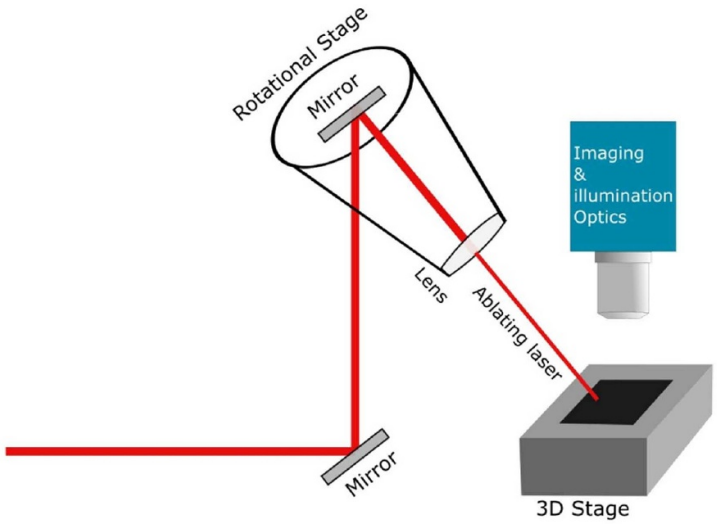

Figure 1. Experimental setup showing how the laser beam is directed through a periscope assembly and subsequently through a lens mounted on a rotation stage.

and 3 for a volume. For non-Euclidean objects, the fractal dimension exhibits non-integer values. In this case, the probability in a certain region (P_i) of a measure scales with the size (ε) of the system as $P_i(\varepsilon) \sim \varepsilon^{\alpha_i}$, where α_i is the Liptschitz–Holder exponent known as the singularity strength of the ith region of the system [14, 15, 18]. By separating the system into boxes of side length ε, we can count the number of boxes with similar singularity strengths. The number of boxes $N(\alpha)$ where the probability (P_i) has a singularity strength between α and $\alpha + \mathrm{d}\,\alpha$ scales as $N(\alpha) \sim \varepsilon^{-f(\alpha)}$ [14, 15, 18], where $f(\alpha)$ is the fractal dimension of the set of boxes with a singularity strength α known as the singularity spectrum.

Experiments were done using an amplified Ti-sapphire laser system with pulse duration of 50 fs, repetition rate of 1 kHz and central wavelength of 800 nm irradiating 1 mm foils of Cu (see figure 1). Laser irradiation was incident at 50-degree and single pulse fluence of 5.48 mJ cm^{-2} [19]. Using a high incidence angle is necessary to obtain herringbone laser-induced periodic surface structure (HLIPSS) [12]. Moreover, as one can see from figure 1, to simultaneously obtain an image of a given position in the sample using a laser scanning microscope and ablate the sample with a femtosecond pulsed laser, the incidence angle must be sufficiently large to avoid beam clipping by the microscope setup. The surface was studied using a UV laser scanning confocal microscope. Images were taken of the same irradiated focal area between bursts of femtosecond pulses. An electromechanical shutter controlled the number of laser pulses (N). Multifractal spectra where computed using the image analysis program imageJ's box counting plugin FracLac [20, 21]. The images were initially binarized into black and white pixels using Make Binary command. The two-dimensional grid position, by which these boxes are laid out, plays an important role in properly measuring the fractal dimension of the image as the number of boxes containing information varies with grid position. To eliminate this ambiguity, multifractal spectrum reported are given as the average over all grid positions.

We analyze the structural evolution of femtosecond laser induced surface structures irradiated at an incident angle of 50 degrees, for various laser polarizations at an absorbed fluence of 5.48 mJ cm^{-2}. Several representative surface structures produced on the Cu are shown in figure 1 for s-polarized, p-polarized, and 45°-polarized irradiation. For s-polarized irradiation, multiple channel formations gradually develop as the pulse number N increases. For $N = 100$–1 k we observe LIPSSs, see figure 2(a) (inset). LIPSS are a 1D periodic structures with a period close to the irradiation wavelength. LIPSSs form due to the interference between scattered surface electromagnetic waves and the incident laser. For metals, LIPSS period is orthogonal to the incident laser polarization [10, 11]. As N increases, several long channels form (figure 2(b)). At 10 k laser pulses, HLIPSS forms within the channels. HLIPSS is a series of nested V-shaped periodic structures which arises due to the formation of grooves which reflect and rotate the projected laser's polarization [12]. As the incident laser reflects from the grooves' walls, the LIPSS orientation rotates and, due to the mirror-symmetry between the grooves walls, create a v-shaped LIPSS (figure 2(c)) [12]. These structures appear parallel to each other in the middle section of the ablated regime. Note that the grooves from due to defect-focused ablation and the grooves direction depends on the laser propagation direction. For p-polarized irradiation, LIPSSs are observed within the first 100 laser pulses (figure 2(d)). As the pulse number increases, LIPSS become hazy and lack uniformity while grooves do not form (figure 2(e)). This is

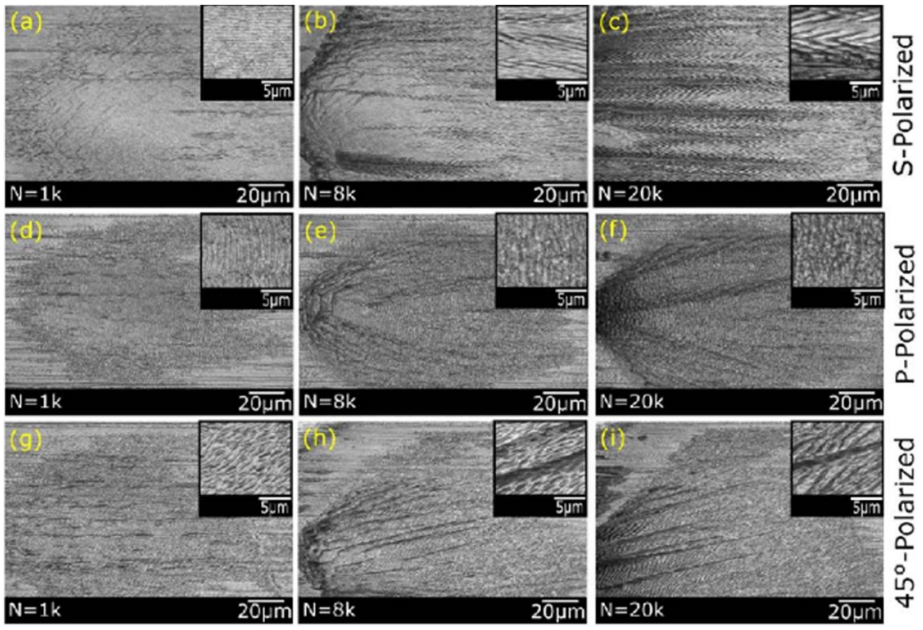

Figure 2. Laser scanning microscope images showing the evolution of laser ablated Cu surfaces after a sequential number of laser pulses (N).

because the formed LIPSS is orthogonal to the laser propagation direction (from left to right for all images), i.e. there exists a competition between the LIPSS formation and channel formation. Consequently, HLIPSS do not appear. Although no structures are observed in the center of the ablated region for p-polarized irradiation, material transport along the laser beam propagation form bow wave shaped sidewalls, (figure 2(f)). Finally, for a 45° polarization irradiation, LIPSSs form with a 45° orientation (figure 2(g)). At large N, nascent grooves are formed which alter their orientation towards the orientation of the LIPSSs that form uniformly along the material surface, (figures 2(h) and (i)). Although channels form, HLIPSS does not due to the changing orientation of the channels [12]. LIPSS created via p-polarized light lack uniformity in our experiments, i.e. the formed LIPSS grating do not have a well-defined orientation across the direction orthogonal to the LIPSS period. This is because the incident laser is at an angle, hence, p-polarized LIPSSs is subject to more direct ablation and material transport which is dominant in the same direction as the LIPSS period.

Figure 3 shows the singularity spectra $f(\alpha)$ as a function of singularity strength α for s, p, and 45° laser polarization from $N = 100$–20 k. For all studied polarizations, the singularity spectra show a pulse number dependent change in the spread of α, which denotes a pulse number dependent spread in the scaling present in the ablated surface morphology. The shape of the multifractal spectrum sheds light on the homogeneity and fractal nature of the analyzed surfaces. $f(\alpha)$ represents the strength of the contribution of each singularity (α).

The width of the singularity spectra ($\alpha_{max} - \alpha_{min}$) indicates the variety of the scaling present in the ablated samples. A system with a large spread in the singularity strength, α, would be rougher or less uniform, i.e. has a greater variation across the system, than a system with a narrow spread in α. Here the wider spread of the singularity spectrum statistically reveals the multifractal nature of the laser induced surfaces. For monofractal images, the singularity spectrum shows no variation mostly a continuous line. As opposed to subjective analysis of the images, multifractal analysis is an objective tool that highlighted the polarization dependence of LIPSS and channel formation on Cu.

Figure 4 shows the difference between the maximum and the minimum values of α as a function of N, i.e. $\Delta\alpha(N)$ for s, p and 45°-polarization. The singularity spectrum shows a pulse number dependent change in the spread of α, which denotes a pulse number dependent spread in the scaling present in the ablated surface morphology.

We observe three distinct dynamical regimes for each of the polarizations studied. In the first regime for the s-polarization ablated surface (figure 4(a)) corresponds to the highest $\Delta\alpha$, which occurs between 100 and 2.5 k laser pulses where the surface is largely covered by LIPSSs. This reveals that the surface complexity is high as the multifractal spectrum shows wider spread. In the second regime, when laser pulses increase from 2.5 to 8 k pulses, channels form which slightly reduces the multifractal scaling on the surface and

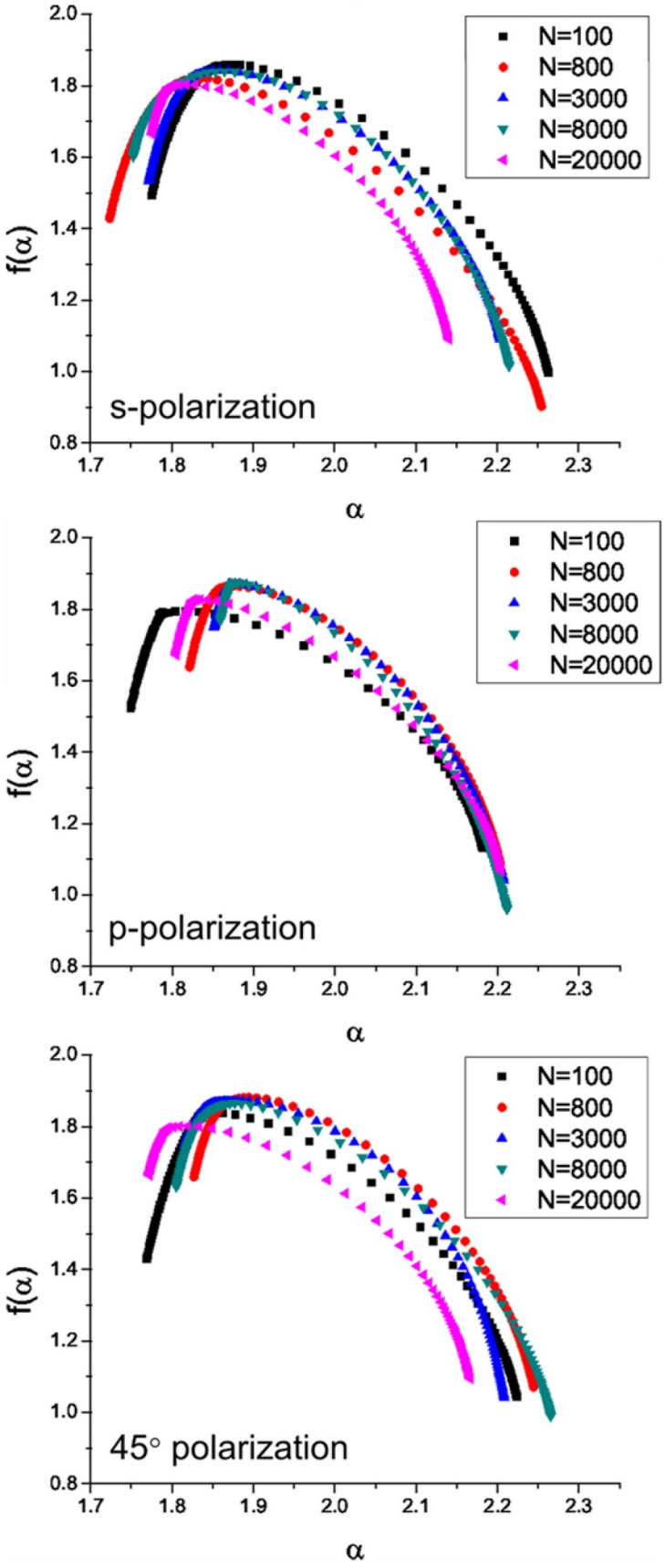

Figure 3. Results of multifractal analyses for s-polarized, p-polarized, and 45°-polarized irradiation. Plots show the multifractal singularity spectrum ($f(\alpha)$) as a function of singularity strength (α), for various number of laser pulses (N).

reflects the smoothened surface morphology compared to the previous regime. Beyond 8 k pulses, in the third region, these channels grow longer and more uniform, and HLIPSS for higher N which consistently

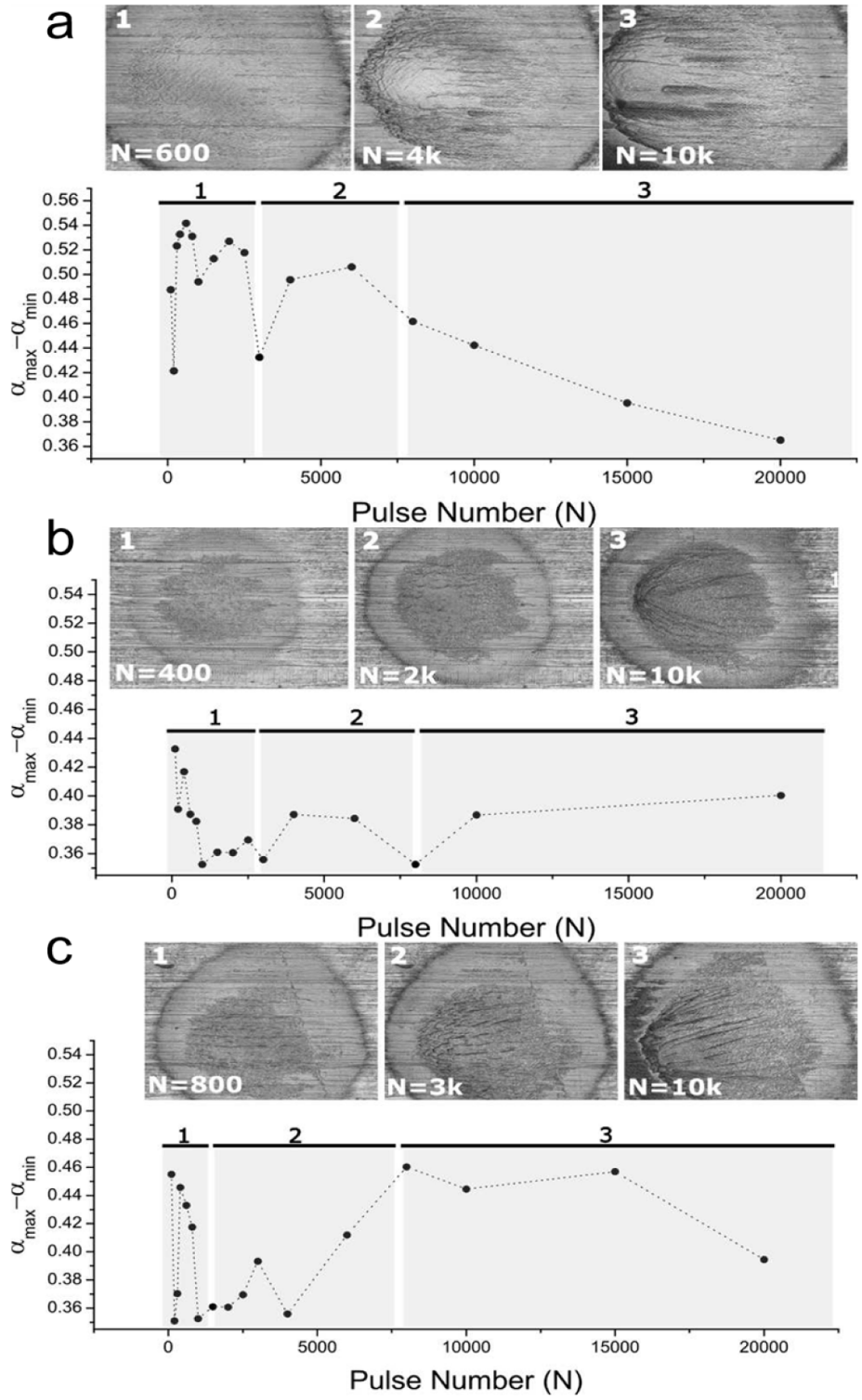

Figure 4. Difference of the singularity spectrum at various laser shot numbers for (a) s-polarized (b) p-polarized and (c) 45°-polarized laser irradiated Cu.

reduces the spread of scaling on the Cu surface. From these it can be conjectured that the laser induced surface dynamics is controlled by the size of the channels. Larger channels decrease the value of $\Delta\alpha$ in the third regime. Hence, we observe a dynamical transition from disordered to a more ordered state.

For p-polarized laser irradiation (figure 4(b)) $\Delta\alpha$ changes incrementally from 100 to 20 k pulses which highlights that no significant change to the surface's morphology is occurring. However, the three distinct regimes of interest remain clearly observed. In the first region, between 100 and 3 k pulses, LIPSS structures cover more surface area with increasing N, making the surface more uniform and reducing the multifractal scaling found on the surface. Between 3 and 8 k pulses, LIPSSs lack uniformity which increases the

multifractal scaling. After 8 k pulses, material transport along the laser beam propagation forms bow wave shaped sidewalls which begins to increase the randomness of the surface which increases $\Delta\alpha$. Figure 4(c) shows the $\Delta\alpha$ for 45°-polarized laser irradiated Cu. Similar to the s-polarized irradiated Cu, between 100 and 1.5 k pulses, LIPSS formations yield a high $\Delta\alpha$ where then, between 1.5 and 8 k pulses, channels begin to form and reorient, which causes an initial decrease in $\Delta\alpha$ followed by a sudden increase as the nascent channels begin to reorient. After 8k pulses, with increasing pulse number, the formed channels achieve their preferred direction and elongate. In this phase, as the direction of the channels changes, $\Delta\alpha$ remains relatively static while the eventual elongation of the channels reduces $\Delta\alpha$. The reduction in $\Delta\alpha$ for 45° is much less than that computed for s-polarized irradiation. This difference in $\Delta\alpha$ after 20 k pulses is likely due to the periodic nature of the HLIPSS formed only for s-polarized irradiation. Channel formations consistently correlate with a decrease in $\Delta\alpha$. A decreased $\Delta\alpha$ indicates that the surface is more uniform, i.e. having less spread in the multifractal scaling. Conversely, LIPSS structures are more repetitive than channel formations, thus, exhibit a larger spread in the multifractal scaling and gives the evidence of multifractlity. Higher multifractal behavior was shown to correlate with a greater surface roughness when studied in relation to surfaces [22]. The performed Multifractal analyses elucidates not only the polarization dependent nature of the structures studied, but also that LIPSSs impart a greater surface roughness than channels. A key insight from the multifractal analyses is that LIPSS formed under s-polarized irradiation, for lower pulse numbers (100–1 k), but a higher spread in multifractal scaling, than does 45° or p-polarized irradiation. This indicates that high incident angle, low pulse number, irradiation from an s-polarized irradiation creates a more uniformly rough surface, i.e. uniform LIPSS, than 45° or p-polarized irradiation. Such insights are not apparent by simply observing images of the surface. This insight may assist future studies on the laser-induced surface functionalization that require uniformly rough surfaces, e.g. for superhydrophobic surfaces [23].

Multifractal analysis enabled us to objectively characterize the laser-dependent morphological properties of HLIPSS. Although Fourier transform analysis of surface structures provides information on the periodicity and dimensionality of the formed periodic surface structures [24], it is difficult to use Fourier transform analysis to analyze randomly formed structures or hierarchical structures. The Multifractal analysis, however, enabled us to assess the hierarchy, uniformity, and roughness of the formed structures and their dependence on the pulse number, polarization and laser pulse properties [25–28]. Objective characterization of laser ablated surfaces allows gaining a deeper understanding of the physics underlying their structural evolution. Future works employing an integrated SEM or AFM microscopy setup with femtosecond laser ablation setup can open the door for investigating the fractal and multifractal analysis of nanoscale structures as well as allowing for quantitative analysis of the physical dimensions of the formed surfaces.

Acknowledgments

US Army Research Office; Bill & Melinda Gates Foundation.

ORCID iDs

Vramori Mitra https://orcid.org/0000-0002-4424-8230
Erik M Garcell https://orcid.org/0000-0002-1375-5184
Anupam Neogi https://orcid.org/0000-0003-0789-1734
Chunlei Guo https://orcid.org/0000-0001-8525-6301

References

[1] Mandelbrot B B 1983 *The Fractal Geometry of Nature* vol 173 (New York: WH Freeman) (https://doi.org/10.2307/2686529)
[2] Turcotte D 1989 A fractal approach to probabilistic seismic hazard assessment *Tectonophysics* **167** 171–7
[3] Iftekharuddin K M, Zheng J, Islam M A and Ogg R J 2009 Fractal-based brain tumor detection in multimodal MRI *Appl. Math. Comput.* **207** 23–41
[4] Davis G M 1998 A wavelet-based analysis of fractal image compression *IEEE Trans. Image Process.* **7** 141–54
[5] Chaudhuri B B and Sarkar N 1995 Texture segmentation using fractal dimension *IEEE Trans. Pattern Anal. Mach. Intell.* **17** 72–77
[6] Ba L, Zen J, Zhang S and Wu Z 1995 Fractals in annealed Ge-Au/Au bilayer films *J. Appl. Phys.* **77** 587–90
[7] Guo B, Sun J, Lu Y and Jiang L 2019 Ultrafast dynamics observation during femtosecond laser-material interaction *Int. J. Extreme Manuf.* **1** 032004
[8] Zhang D, Ranjan B, Tanaka T and Sugioka K 2020 Underwater persistent bubble-assisted femtosecond laser ablation for hierarchical micro/nanostructuring *Int. J. Extreme Manuf.* **2** 015001
[9] Vorobyev A Y and Guo C 2013 Direct femtosecond laser surface nano/microstructuring and its applications *Laser Photon. Rev.* **7** 385–407
[10] Bonse J, Höhm S, Kirner S V, Rosenfeld A and Krüger J 2016 Laser-induced periodic surface structures—a scientific evergreen *IEEE J. Sel. Top. Quantum Electron.* **23** 1

[11] Jalil S A, Yang J, ElKabbash M, Singh S C and Guo C 2019 Maskless formation of uniform subwavelength periodic surface structures by double temporally-delayed femtosecond laser beams *Appl. Surf. Sci.* **471** 516–20
[12] Garcell E M, Lam B and Guo C 2018 Femtosecond laser-induced herringbone patterns *Appl. Phys.* A **124** 405
[13] Zheng X, Cong C, Lei Y, Yang J and Guo C 2018 Formation of slantwise surface ripples by femtosecond laser irradiation *Nanomaterials* **8** 458
[14] Vicsek T 1992 *Fractal Growth Phenomena* (Singapore: World scientific) (https://doi.org/10.1142/1407)
[15] Tél T 1988 Fractals, multifractals, and thermodynamics *Z. Naturforsch.* A **43** 1154–74
[16] Pietronero L and Tosatti E 2012 *Fractals in Physics* (Amsterdam: Elsevier)
[17] Falconer K J 1986 *The Geometry of Fractal Sets* vol 85 (Cambridge: Cambridge University Press) (https://doi.org/10.1017/CBO9780511623738)
[18] Chhabra A and Jensen R V 1989 Direct determination of the f(α) singularity spectrum *Phys. Rev. Lett.* **62** 1327
[19] Jackson J D 2007 *Classical Electrodynamics* (New York: Wiley)
[20] Schneider C A, Rasband W S and Eliceiri K W 2012 NIH image to imagej: 25 years of image analysis *Nat. Methods* **9** 671–5
[21] Karperien A 1999–2013 FracLac for ImageJ (Charles Sturt University) (http://rsb.info.nih.gov/ij/plugins/fraclac/FLHelp/Introduction.htm)
[22] Chaudhari A, Yan -C-C S and Lee S-L 2004 Multifractal analysis of growing surfaces *Appl. Surf. Sci.* **238** 513–7
[23] Jalil S A, Lai B, ElKabbash M, Zhang J, Garcell E M, Singh S and Guo C 2020 Spectral absorption control of femtosecond laser-treated metals and application in solar-thermal devices *Light Sci. Appl.* **9** 1–9
[24] Lei Y, Yang J, Cong C and Guo C 2020 Fabrication of homogenous subwavelength grating structures on metallic glass using double-pulsed femtosecond lasers *Opt. Lasers Eng.* **134** 106273
[25] Pawliszewska M, Ge Y, Li Z, Zhang H and Sotor J 2017 Fundamental and harmonic mode-locking at 2.1 μm with black phosphorus saturable absorber *Opt. Express* **25** 16916–21
[26] Yan P, Lin R, Chen H, Zhang H, Liu A, Yang H and Ruan S 2014 Topological insulator solution filled in photonic crystal fiber for passive mode-locked fiber laser *IEEE Photon. Technol. Lett.* **27** 264–7
[27] He J, Tao L, Zhang H, Zhou B and Li J 2019 Emerging 2D materials beyond graphene for ultrashort pulse generation in fiber lasers *Nanoscale* **11** 2577–93
[28] Vorobyev A and Guo C 2010 Water sprints uphill on glass *J. Appl. Phys.* **108** 123512